Journal of Alloys and Compounds 1043 (2025) 184229

Contents lists available at ScienceDirect

Journal of Alloys and Compounds

journal homepage: www.elsevier.com/locate/jalcom

Crystallization effect in the self-bias response of several Fe-rich magnetoelastic alloys

Ana Catarina Lopes [a,b,*], J. Gutiérrez [c,d], A. García-Arribas [c,d], A. Aginagalde [e], A. Ayerdi [e], I. Quintana [f], J.L. Vilas [a,d], J.S. Garitaonandia [c,**], A. Lasheras [c,**]

[a] Macromolecular Chemistry Group (LABQUIMAC), Department of Physical Chemistry, Faculty of Science and Technology, University of the Basque Country, UPV/EHU, Barrio Sarriena s/n, Leioa 48940, Spain
[b] IKERBASQUE, Basque Foundation for Science, Plaza Euskadi 5, Bilbao 48009, Spain
[c] Faculty of Science and Technology, University of the Basque Country (UPV/EHU), Barrio Sarriena s/n, Leioa 48940, Spain
[d] BCMaterials, Basque Center for Materials, Applications and Nanostructures, UPV/EHU Science Park, Leioa 48940, Spain
[e] Mechanics and Industrial Production, Faculty of Engineering, Mondragon Unibertsitatea, Loramendi 4, Mondragon 20500, Spain
[f] Tekniker, Basque Research and Technology Alliance (BRTA), C/Iñaki Goenaga 5, Eibar 20600, Spain

A B S T R A C T

This work investigates the self-bias effect in thermally annealed Fe-based magnetoelastic sensors, extending previous findings on Vitrovac® 7600 to compositions designed for enhanced corrosion resistance. The alloys FeNiCrSiB, FeCoSiB, and Metglas were selected to evaluate the influence of annealing-induced crystallization on their magnetic, magnetoelastic, structural, and electrochemical properties, with a focus on their suitability for operation in harsh environments. The results reveal that thermal treatment at 500 °C resulted in partial crystallization, as confirmed by X-ray diffraction and Mössbauer spectroscopy, yielding a dual-phase structure composed of crystalline and amorphous regions. In addition, all treated samples exhibited stable and clearly detectable self-bias magnetoelastic resonances after one month, as well as significant improvements in quality factor (up to 1050 for the FeCoSiB alloy) and frequency stability over time (maximum deviation down to 6 and 12 Hz for the Metglas and FeCoSiB sensors, respectively). Further, while thermal annealing adversely affected the corrosion resistance of V7600 and FeCoSiB (increase in the corrosion rate of 76 % and 660 %, respectively), it preserved the stability of Metglas and substantially improved the performance of FeNiCrSiB (55 % reduction in corrosion rate). These results highlight the potential of Cr- and Ni-enriched Fe-based alloys as suitable candidates for self-bias magnetoelastic sensor platforms to be employed in harsh environments.

1. Introduction

The use of magnetoelastic (ME) platforms in the development of the new generation of mass sensors has experienced a significant growth in the last years. The advances carried out in the mass sensitivity and their employment in the detection of different biological and chemical agents, as well as monitoring of several other processes have clearly demonstrated the potential of this kind of sensors [1]. Nevertheless, they have yet to attract substantial market interest and remain below the threshold of commercial viability, where enhanced mass sensitivity and the simplification of the system are crucial requirements for large-scale industrial adoption. Concerning the sensitivity of the sensor, the efforts in the last years have been focused on two different strategies: reduction of the dimensions of the sensors [2,3] and geometry engineering [4–6]. In both cases, an increase of the resonance frequency is obtained, which is directly reflected in a rise of the sensitivity [1]. Regarding the integration of the ME sensors, the attention has been focused on the miniaturization and optimization of the assembly [7,8].

Recently, our group drew attention to an effect that contributes both to improve the sensitivity of the mass sensor and to simplify and compact the measurement setup [9]. The crystallization induction through the thermal annealing reported in the Vitrovac® 7600 T70 ribbons showed an increase of 40 % in the mass sensitivity with respect to the as-quenched one. In addition, that crystallization induced a self-bias response resulted from the appearance of the magnetically hard FeCo and Fe_2B compounds, which, after the platforms were pre-magnetized with a permanent magnet, they generated their own bias field. A diagram of this effect is shown in Fig. 1.

The self-bias response represents a significant advancement in the integration of ME sensors into a wide range of applications, as it

* Corresponding author at: Macromolecular Chemistry Group (LABQUIMAC), Department of Physical Chemistry, Faculty of Science and Technology, University of the Basque Country, UPV/EHU, Barrio Sarriena s/n, Leioa 48940, Spain.
** Corresponding authors.
E-mail addresses: anacatarina.lopes@ehu.eus (A.C. Lopes), js.garitaonandia@ehu.eus (J.S. Garitaonandia), andoni.lasheras@ehu.eus (A. Lasheras).

https://doi.org/10.1016/j.jallcom.2025.184229
Received 30 July 2025; Received in revised form 16 September 2025; Accepted 5 October 2025
Available online 6 October 2025

eliminates the need for an external DC magnetic field. The sensor instead generates the required DC component internally, which significantly simplifies the sensing process and requires only the application of a small AC magnetic field for effective operation. Thus, it represents a further step toward the development of a simplified and compact system that enables fast, accurate, and user-friendly detection of various external agents.

ME sensors, which are widely employed for detecting biological and chemical agents [10–14], monitoring glucose levels [15,16], and measuring the viscosity of different substances [17], are often exposed to harsh and corrosive environments. Under such conditions, corrosion resistance becomes a critical factor for a long-term performance. In such cases, ME ribbons are typically alloyed with elements such as Ni or Cr to enhance durability and prevent oxidation of the active material [18,19]. That is the case of the commercial Metglas ribbon, widely used in the detection of biological parameters [12,13]. Thus, extending the investigation of thermal treatments that lead to the self-bias effect to Fe-rich alloys with enhanced corrosion resistance could open new possibilities for the development of robust and versatile sensor designs.

This study aims to investigate the self-bias response induced by thermal annealing in Fe-based ME alloys, particularly those designed for harsh environments, and to analyze how such treatments influence their corrosion resistance. The previously reported results for Vitrovac® 7600 T70 [9] will be used for comparison. This composition is expected to exhibit low corrosion resistance. The analyzed alloy compositions were selected to maintain a similar relative quantity of magnetic atoms, ranging from 78 at% in $Fe_{54}Ni_{24}Cr_2Si_{10}B_{10}$ to 83 at% in Vitrovac® 7600 T70 ($Fe_{65}Co_{18}Mo_{0.3}Si_{0.8}B_{15.5}C_{0.4}$). Each alloy was chosen to highlight a specific property relevant to magnetoelastic sensing: (i) FeNiCrSiB incorporates Cr and Ni, elements well-known to enhance corrosion resistance, making it a promising candidate for harsh environments [18,20,21]; (ii) FeCoSiB contains a high Co content, which increases magnetization and magnetostriction; (iii) Metglas 2826 ($Fe_{37}Ni_{42}Mo_4B_{17}$) is widely used in mass sensing due to its excellent corrosion resistance and soft magnetic behaviour [1]. This selection therefore enables a systematic comparison between alloys with contrasting corrosion resistance and magnetic responses, while maintaining similar magnetic atoms. For all the alloys, calorimetry measurements were carried out to identify phase transition temperatures. In addition, the structural characterization were performed to determine the different phases formed after crystallization. Finally, magnetic and ME measurements were carried out to quantify the self-bias ME resonance response, and the impact of thermal treatments on the corrosion resistance of each sample was also evaluated.

2. Experimental methods

The alloys with compositions $Fe_{54}Ni_{24}Cr_2Si_{10}B_{10}$, $Fe_{64}Co_{17}Si_{6.6}B_{12.4}$ and $Fe_{65}Co_{18}Mo_{0.3}Si_{0.8}B_{15.5}C_{0.4}$ (in the following FeNiCrSiB, FeCoSiB and V7600, respectively) were obtained from Vacuumschmelze, while the Metglas alloy (with composition $Fe_{37}Ni_{42}Mo_4B_{17}$) was sourced from Metglas. The densities for the alloys were 7350 kg/m^3, 7900 kg/m^3, 7350 kg/m^3 and 7480 kg/m^3 for the FeNiCrSiB, Metglas, FeCoSiB, and V7600, respectively. All the studied alloys had a thickness of approximately 20 μm. Rectangular strips with dimensions of 25 mm × 2 mm were prepared using femtosecond laser ablation (MONACO: COHERENT, integrated into a micromachining workstation: microSTRUCTvario, 3D-Micromac, AG, Germany). The laser system operated at 15 W with a wavelength of 517 nm, a frequency of 750 kHz, and a scanning speed of 1500 mm/s. This technique is not expected to induce any variation in the alloy structure [9], and any minor surface effects are inherently accounted for in the corrosion measurements. A summary of the analyzed materials and their composition is shown in Table 1:

To determine the thermal transitions of the materials, Differential Scanning Calorimetry (DSC) was performed using a Mettler Toledo DSC 822e calorimeter. Approximately 17 mg of each sample was sealed in aluminium capsules and subjected to a temperature range of 25–600 ºC at a heating rate of 25 ºC/min under a nitrogen flow of 20 mL·min^{-1} .

After determining the crystallization temperature, the alloys were annealed for 30 min in a furnace and subsequently cooled down to room temperature.

The crystallized phases were obtained through X-ray powder diffraction (XRD) using a Panalytical X´pert PRO diffractometer with CuKα radiation. Room-temperature ^{57}Fe Mössbauer spectroscopy was conducted using a conventional constant-acceleration spectrometer in transmission geometry, with a ^{57}CoRh source (nominal activity 24 mCi, March 2024). Isomer shifts and calibration were referenced to α-Fe at room temperature, and the spectra were analyzed using the NORMOS software package developed by Brand [23]. Mössbauer spectroscopy was utilized to assess the degree of crystallization of the sensors and to verify the structure and composition of the crystallized phases.

The magnetic properties of the alloys were investigated using an inductive hysteresis loop tracer. The magnetic field was produced by Helmholtz coils powered by a bipolar supply (KEPCO BOP 20–20 M). The field strength was calculated from the voltage drop across a standard resistor, with a conversion factor of 30.4 Oe·A^{-1} .

ME characterization for as-quenched alloys was conducted using a custom-built setup. Two coaxial solenoids provided the DC and AC magnetic fields required to drive the samples to resonance and enhance the signal. Inside the solenoids, a pick-up coil was arranged in series

Table 1
Summary of the analyzed alloys and their main characteristics.

Label	Composition	Characteristics	References
V7600	$Fe_{65}Co_{18}Mo_{0.3}Si_{0.8}B_{15.5}C_{0.4}$	Sensor tested in a previous study. It will be used as a reference in this work. High magneto-mechanical coupling.	[9]
FeCoSiB	$Fe_{64}Co_{17}Si_{6.6}B_{12.4}$	Traditionally used in magnetoelectric composites. High magneto-mechanical coupling.	[22]
Metglas	$Fe_{37}Ni_{42}Mo_4B_{17}$	Used for biological and chemical detection systems. High corrosion resistance.	[10–14]
FeNiCrSiB	$Fe_{54}Ni_{24}Cr_2Si_{10}B_{10}$	High corrosion resistance.	[18,20,21]

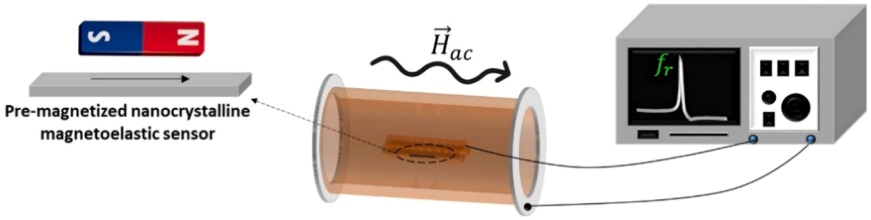

Fig. 1. Diagram of the self-bias effect in crystalline magnetoelastic sensors.

with a compensating coil, and the induced voltage was monitored using an HP 3589 A spectrum analyzer and recorded on a computer. The procedure for crystallized sensor was the same, but disconnecting the DC source (i.e. without DC bias field). This ME setup allowed us to precisely determine the resonant frequency of each sensor. From that value, the Young's modulus corresponding to the first vibration mode was calculated through Eq. (1):

$$E(H) = \rho(2Lf_r)^2 \quad (1)$$

where, ρ is the density of the ME ribbon, f_r the resonant frequency and L its length. The sharpness of the resonances was quantified through the quality factor Q, a key parameter in mass sensors. This parameter is calculated through the expression $Q = f_r/\Delta f$, being f_r the resonance frequency value and Δf the frequency difference at the half maximum intensity. Finally, the ME coupling coefficient was obtained using Eq. (2):

$$k = \sqrt{\frac{\pi^2}{8}\left[1 - \left(\frac{f_r}{f_a}\right)^2\right]} \quad (2)$$

where f_a the antiresonance frequency.

Potentiodynamic polarization tests were performed in a three-electrode electrochemical cell using a 3.5 wt% NaCl aqueous solution to simulate a corrosive environment. A pure platinum wire served as the counter electrode, and a saturated calomel electrode (SCE) was used as the reference electrode. Prior to polarization, the open circuit potential (OCP) was monitored for 10 min to allow stabilization. Polarization scans were then carried out from –500 mV to + 500 mV versus OCP at a scan rate of 1 mV/s. All measurements were conducted using a Voltalab PGZ 301 potentiostat.

3. Results and discussion

The fabricated as-quenched alloys were firstly magnetically and magnetoelastically characterized by measuring the hysteresis loops, and resonance frequencies under a range of DC magnetic field values. From the resonance frequencies, both Young's modulus curve and ME coupling coefficient were determined. The resonance curves were measured at the magnetic field corresponding to the minimum of the Young's modulus, H_{min}. The results are represented in Fig. 2:

From Fig. 2, we have determined the main magnetic and magnetoelastic parameters of the sensors, summarized in Table 2:

As was previously mentioned, these alloys show varied magnetic and magnetoelastic properties, significantly influenced by the inclusion of elements such as Cr or Ni. The inclusion of those elements, in spite of providing anticorrosive properties, has a negative impact in the saturation magnetization and saturation magnetostriction. In addition, the incorporation of Cr dissipates the ME coupling, with a maximum value of 0.05 for the alloy containing Cr. That is translated into a reduction of the signal intensity, as can be observed in Fig. 2(d). However, ME resonances can be perfectly measured for all the analyzed ribbons with precision.

In the recent work reported by our group [9], the self-bias effect was a consequence of the nanocrystallization of the V7600 sensor, which was successfully carried out through its thermal annealing at 550ºC. In order to determine the thermal annealing of the new alloys to be studied, DSC measurements were performed. This technique allows us to observe the phase transformations through the exothermic peaks. The results are

Table 2
Saturation magnetization $\mu_0 M_s$, minimum of the Young's modulus E_{min}, magnetic field at the minimum value of the Young's modulus H_{min}, maximum value of magnetoelastic coupling coefficient k_{max}, resonance frequency and quality factor values measured at H_{min}, and saturation magnetostriction λ_s of the analyzed sensors. The values for the saturation magnetostriction have been obtained from the literature.

Sensor	$\mu_0 M_s$ (T)	E_{min} (GPa)	H_{min} (Oe)	k_{max}	f_r (kHz)	Q	λ_s (ppm)
FeNiCrSiB	0.7	146	8	0.05	89.2	469	11.5 [19]
Metglas	0.9	153	7	0.26	88.0	204	12 [1]
FeCoSiB	1.7	141	4	0.13	87.7	115	20.5 [19]
V7600	1.6	120	8	0.45	80.0	60	42 [9]

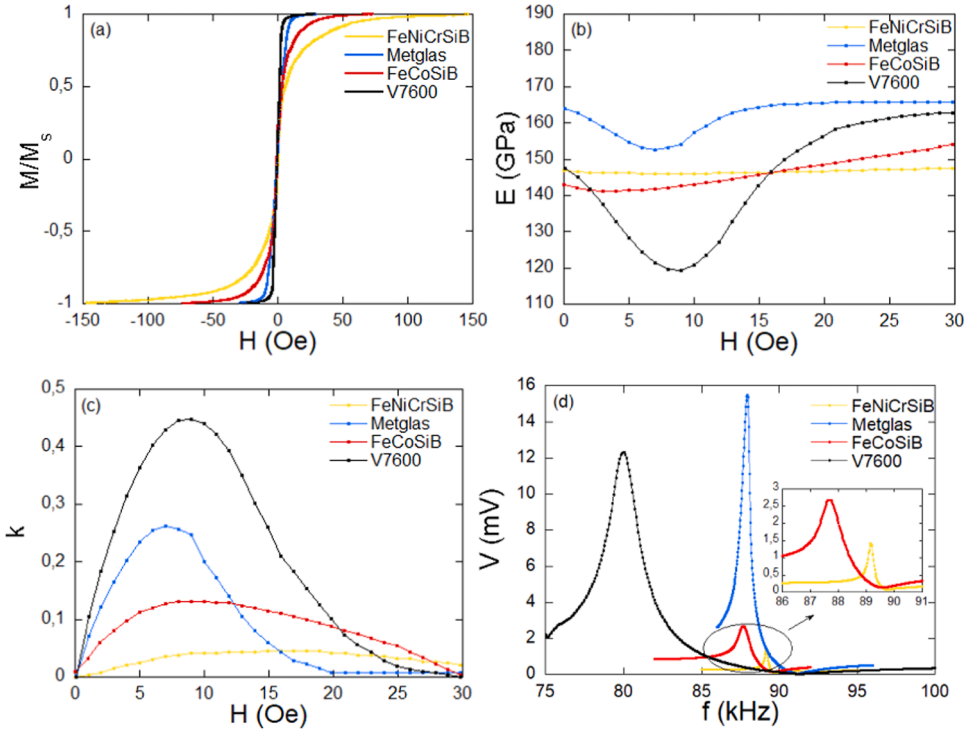

Fig. 2. (a) Normalized hysteresis loop, (b) Young's modulus, (c) magnetoelastic coupling coefficient and (d) magnetoelastic resonances of the analyzed alloys.

shown in Fig. 3:

All analyzed compositions exhibit two exothermic peaks. These pronounced exothermic behaviors are likely attributed to phase transformations associated with the formation of stable crystalline phases. The first peak, occurring between 400°C and 500°C depending on the alloy, is likely related to a partial crystallization process. Similar to the V7600 sample, the primary crystallization is expected to involve a magnetic Fe(Co)(Ni)-rich phase, while the higher-temperature exothermic peaks is expected to correspond to the formation of borates [9].

Although we initially intended to perform treatments at temperatures above the second crystallization stage (550 °C), issues related to the structural integrity of the ribbons were encountered, leading to their deterioration. In addition, since there is a temperature interval between both crystallization processes, the coexistence of the primary crystallized Fe(Co)(Ni)-rich phase with a remaining amorphous phase is anticipated in all three samples. For this reason, the heat treatment was limited to 500 °C, which is expected to induce the necessary crystallization for the self-bias effect while remaining sufficiently below the second crystallization peak to ensure a similar final microstructure among the three treated alloys.

Fig. 4 presents the X-ray diffractograms obtained from the annealed FeNiCrSiB, FeCoSiB, and Metglas alloys. For comparison, the diffractogram of the fully crystallized V7600 alloy annealed at 550°C is also included:

As observed, the annealed FeNiCrSiB and FeCoSiB alloys exhibit diffraction patterns at approximately 45.0°, 65.4°, and 82.8°, corresponding to the [110], [200], and [211] crystallographic reflections of a body-centered cubic (bcc) structure. These peaks are slightly shifted from those expected for pure α-Fe, indicating the incorporation of additional elements into the structure. The diffractogram of the annealed FeNiCrSiB alloy also displays additional peaks at 46.9°, and 56.5°, which can be attributed to traces of $Cr_3Ni_5Si_2$ and Fe_2B phases, respectively.

In contrast, the Metglas alloy annealed at 500°C exhibits broad peaks at 43.5°, 50.5° and 74.8° associated, respectively, to [111], [200] and [220] Miller indices of a crystalline face-centered cubic (fcc) FeNi alloy. The presence of a fcc structure is characteristic of FeNi alloys with Ni content above 50 at%, consistent with the relative Fe/Ni ratio in the initial Metglas alloy.

The crystallization undergone by the samples after their annealing was also studied through the transmission Mössbauer spectroscopy. This technique provides an accurate assessment about the crystallized fraction of the sample and provides more precise characterization of the amorphous and crystalline components which allows a structural verification of the different coexisting phases and estimation of their composition. Fig. 5 shows the Mössbauer spectra corresponding to FeNiCrSiB and FeCoSiB and Metglas alloys annealed at 500°C.

As it can be observed, Mössbauer spectra of the three alloys show

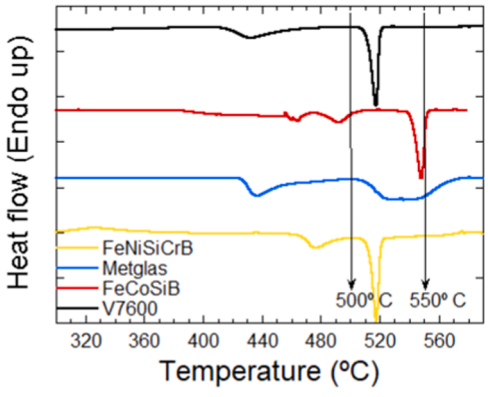

Fig. 3. Differential scanning calorimetry for all the analyzed alloys.

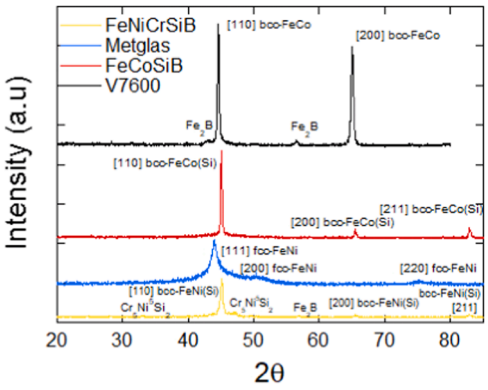

Fig. 4. x-ray diffractograms of the annealed at 500 C FeNiCrSiB and FeCoSiB and Metglas alloys and V7600 alloy annealed at 550 C.

discernible discrete crystalline contributions coexisting with a broad spectral component characteristic of an amorphous magnetic phase, which has been fitted by means of a hyperfine field distribution. These discrete sextets reflect different chemical environments of Fe atoms in the crystalline cubic phase, being their decreasing hyperfine field value associated to the increasing presence of Si in their neighbourhood. The crystalline contribution to the Mössbauer spectrum of the FeNiCrSiB and FeCoSiB can be properly fitted with only three and two, respectively, components, compatible with the presence of Si atoms in a solid solution bcc structure and which would account to Fe atoms with 0 (A8), 1 (A7) and 2 (A6) Si atoms in their neighbourhood for the case of the FeNiCrSiB annealed alloy, and 0 (A8) and 1 (A7) Si atoms for the case of Fe in the crystalline phase of FeCoSiB annealed alloys. In contrast to the X-ray diffractogram, which is a surface-sensitive technique, there was no evidence of the presence of Fe_2B in the Mössbauer spectrum of the FeNiCrSiB annealed alloy, suggesting that its presence may be confined to the sample's surface [24,25]. The hyperfine field values of the A8 component (33.7 T for FeNiCrSiB and 35.4 T for FeCoSiB) are significantly higher than expected for an A8 environment composed solely of Fe atoms. This confirms the incorporation of Ni and Co atoms, respectively, within the crystalline phase, forming a solid solution bcc structure alongside Fe and Si atoms. Fitting results further reveal that 29 % of Fe atoms in the annealed FeNiCrSiB sample reside in the bcc FeNiSi phase, whereas this figure decreases to 20 % for Fe atoms in the bcc FeCoSi phase of the annealed FeCoSiB sample.

For fitting the Mössbauer spectra of Metglas alloys annealed at 500°C, we also employed a procedure that combines binomially distributed discrete spectra for the fcc-FeNi crystalline phase with a distribution of hyperfine fields for the remaining amorphous phase. In an fcc-ordered FeNi alloy, the variations in the nearest-neighbor environment of Fe atoms depend on the number of surrounding Ni atoms, ranging from 0 to 12. This results in up to 13 distinct local environments, where the hyperfine field of the corresponding Fe decreases as the number of Ni atoms in the vicinity increases [26]. The relative probability of each environment is determined by the actual Ni content in the fcc-FeNi crystal. To optimize the fitting process, we excluded spectral components contributing less than 3 % of the total resonant area. Consequently, the contribution of the fcc-FeNi crystalline phase to the Mössbauer spectrum of Metglas alloys annealed at 500°C can be effectively represented by five distinct subspectral components, corresponding to environments with 4 to 8 Ni atoms in the nearest-neighbor shell of Fe atoms. The analysis of the resonant areas obtained from the fitting is consistent with the Fe/Ni ratio in the initial amorphous composition. Moreover, the results indicate that 31 % of the Fe atoms are in the crystalline phase.

Thus, the Mössbauer spectroscopy characterization confirms that the FeNiCrSiB, FeCoSiB, and Metglas alloys annealed at 500°C exhibit similar crystalline-to-amorphous phase fractions. The added Cr, Ni, or

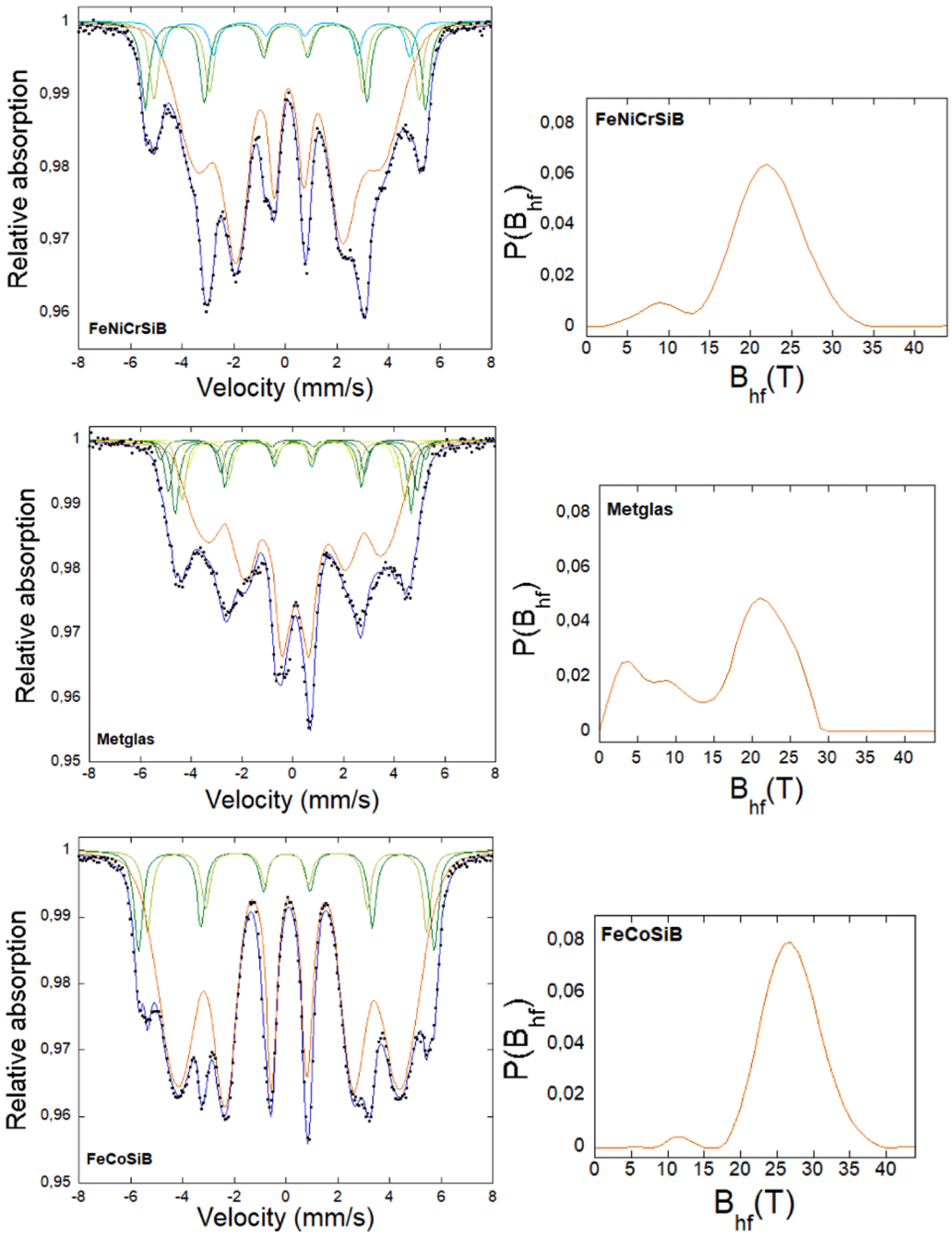

Fig. 5. Mössbauer spectra of the FeNiCrSiB and FeCoSiB and Metglas alloys annealed at 500°C, along with the profile of their hyperfine distributions is presented.

Co atoms are appropriately distributed across both phases, albeit with variations in crystalline phase compositions. This finding provides a solid framework for analyzing the self-bias effect on the magnetoelastic properties of these alloys.

After completing the structural characterization, we carried out a magnetic analysis of the crystallized sensors by measuring their magnetic hysteresis loops and the evolution of the Young's modulus under an applied magnetic field. This magnetic characterization enables a direct comparison with the as-quenched sensors. The results are presented in Fig. 6:

As observed in the hysteresis loops (Fig. 6(a)), the crystallization induced by thermal annealing has significantly influenced the magnetic properties of the materials. All the treated materials present a widening of the hysteresis loop when compared with the non-treated samples (represented in Fig. 2a), attributed to the presence of the crystalline phase, as X-ray and Mössbauer spectra reveal. The FeNiCrSiB sample exhibits the widest hysteresis loop compared to the others, likely due to the presence of bcc FeNiSi phase in its structure. Actually, the incorporation of Si and Cr into the crystal structure intrinsically increases coercivity by modulating the anisotropy constant [27]. In this context, a small increases in crystal size can lead to significant increases in coercive field. This effect is not observed in partially crystallized samples with similar compositions that contain little to no Si and Cr [28,29]. In contrast, materials like Metglas and FeCoSiB show narrower loops, reflecting their softer magnetic nature with lower coercivity and easier magnetization processes. Regarding the remanent magnetization, the crystallized FeCoSiB and V7600 alloys exhibit the highest values, due to their high Co content [30]. These curves are consistent with the Mössbauer spectra shown in Fig. 5.

The dependence of Young's modulus on the applied DC magnetic

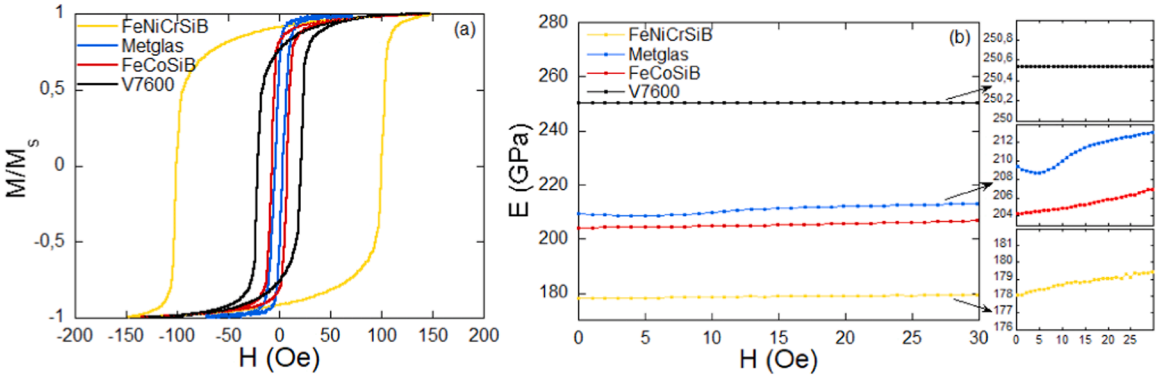

Fig. 6. (a) Normalized hysteresis loops and (b) Young's modulus of the alloys under the applied DC magnetic field.

field, as shown in Fig. 6(b), confirms a significant reduction, and in some cases a near-complete suppression, of its variation as a consequence of crystallization. In addition, the annealing process results in a rise in the Young's modulus value if compared with the as-quenched alloys of Fig. 2(b), indicating an enhancement in the material's stiffness due to structural modifications induced by heat treatment of the alloys. This behavior is directly related to the formation of an intrinsic DC magnetic field by the crystallized alloy itself when the sensors are pre-magnetized, a phenomenon previously referred to as the self-bias effect. Because the material already possesses an internal bias field, the application of an external DC magnetic field does not produce any significant additional effect on the system, resulting in a constant Young's modulus value [9]. This lack of variation in Young's modulus with changes in the external DC magnetic field is more pronounced in the V7600 and FeNiCrSiB samples, as they exhibit higher magnetic coercivity.

Finally, the self-bias effect and its stability over time was analyzed. The crystallized alloys were pre-magnetized with a permanent magnet, and introduced in the ME measurement set-up described in the experimental section. The DC source was disconnected and ME resonance frequency curves were monitored just after pre-magnetizing (day 0) and after one month (day 30). The obtained results are represented in Fig. 7.

As can be appreciated, the resonance frequency of all the alloys can be perfectly detected after 30 days, indicating a strong self-bias effect that stabilizes over time. In addition, an important increase in the quality factor Q of the resonances can be appreciated if compared with as quenched resonances showed in Fig. 2(d), with values that range from 880 up to 1080 (see Table 2). This phenomenon was previously reported by our group [9] for the V7600 alloy. In this work, we have extended these findings to different alloys, which can be applied in various environments depending on the specific application and requirements. However, the intensity of the resonance frequency significantly varies from one alloy to another. The resonance curves of the FeNiCrSiB alloy are significantly noisier and exhibit a much lower amplitude than the other samples. This behavior is likely associated with its higher coercive field, which hinders the ME response by restricting domain wall motion and increasing magnetic losses. The V7600 alloy also presents a relatively high coercivity value, which contributes to its lower induced voltage when compared to Metglas and FeCoSiB alloys. On the contrary, the Metglas and FeCoSiB alloys exhibit the highest induced signal amplitudes, consistent with their lower coercivity and softer magnetic character. This lower coercivity facilitates domain wall motion under AC excitation, resulting in larger magnetization changes and, consequently, higher induced voltages. Furthermore, the alloys with higher coercivity (FeNiCrSiB and V7600) also show more stable self-bias signals after one month, since stronger pinning of domain walls reduces fluctuations and stabilizes the internal bias field, unlike the Metglas and FeCoSiB alloys, which exhibited small reductions of 8 % and 6 %, respectively. Table 3 summarizes the main magnetic and magnetoelastic parameters of the crystallized sensors.

Furthermore, the consistency of the output signal was evaluated in terms of short-term fluctuations. This process has been demonstrated to be crucial in the performance of ME sensors [21]. A stable resonance frequency is essential for ensuring reliable and repeatable sensor responses and improving its accuracy. To quantify these, the variation of resonance frequency over time for all the as-quenched and thermally treated samples was tracked. For the as-quenched alloys, the monitoring

Table 3
Coercive field (H_c), remanent magnetization ($\mu_0 M_r$), resonance frequency (f_r), Young's modulus (E), and quality factor (Q) of the crystallized sensors.

Crystallized sensor	H_c (Oe)	$\mu_0 M_r$ (T)	f_r (kHz)	E (GPa)	Q
FeNiCrSiB	100	0.67	106	206	880
Metglas	4	0.59	103	209	940
FeCoSiB	7	1.30	105	203	1050
V7600	20	1.18	116	252	1080

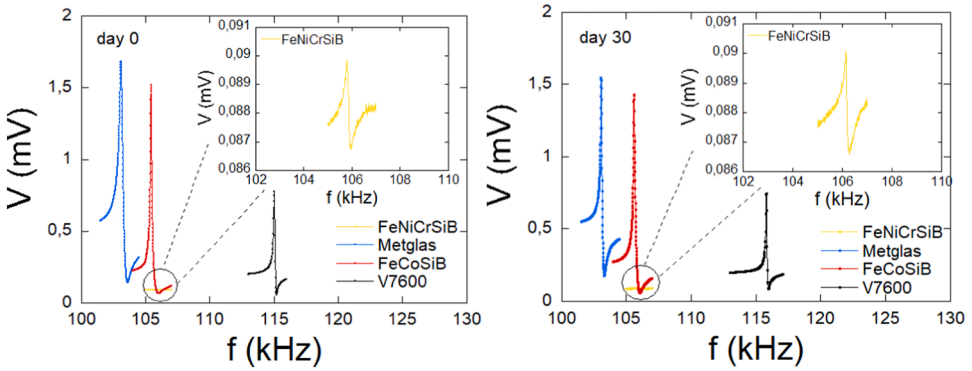

Fig. 7. ME resonance frequencies of the crystallized sensors after being pre-magnetized (left) and after one month (right).

process was performed by setting the resonance frequency value at the H_{min} magnetic field from Table 2 and measuring the variation in the resonance frequency (Δf) for approximately 15 min (900 s). For the thermally treated alloys, since a DC source is not required, we simply pre-magnetized the alloys with a permanent magnet and set the resonance frequency value to that in Table 2. Subsequently, we monitored Δf over the same period of time. The results are shown in Fig. 8:

As can be observed, the as-quenched alloys generally exhibit less stable resonance frequency than the thermally treated ones. In particular, the as quenched FeNiCrSiB, FeCoSiB, and V7600 alloys show maximum deviations exceeding 40 Hz. In contrast, the Metglas alloy displays a much smaller Δf variation of only 4 Hz. This is likely due to its well-defined resonance (see Fig. 2(d)), and a more homogeneous microstructure, with lower internal stresses [31], as also corroborated by its Young's modulus curve (see Fig. 2(b)). However, the results differ when compared to the thermally treated alloys. The deviation for crystallized sensors range from 4 Hz up to 30 Hz for the Metglas, FeCoSiB and FeNiCrSiB compositions, respectively. This improved stability can be attributed to the refined microstructure and reduced internal stresses resulting from the crystallization process. However, the highest stability is still the one exhibited by the V7600, and previously reported [9], which shows an outstanding maximum Δf variation of only 2 Hz. This highest stability is due to the fully crystallized structure, which minimizes internal stresses and reduces variations in mechanical properties. In contrast, partially crystallized alloys may retain amorphous regions, which can introduce heterogeneities in the microstructure and result in less stable resonance frequencies.

Finally, the corrosion resistance of the as quenched and thermally treated samples was analyzed using potentiodynamic polarization measurements, with the aim of evaluating key parameters such as the corrosion potential E, corrosion current density ($i_{corrosion}$), anodic Tafel slope (β_a), and polarization resistance (R_p). This analysis is particularly relevant for the Metglas and FeNiCrSiB alloys, as they are commonly employed in environments where corrosion is a major concern. The obtained results are represented in Fig. 9 and Table S1 of the supplementary information.

For V7600, the treatment led to a deterioration in most corrosion-related parameters, especially $i_{corrosion}$ and β_a, despite a slight increase in polarization resistance. This corresponded to a 76 % increase in corrosion rate and a 23 % rise in corrosion tendency. FeCoSiB exhibited the most pronounced degradation, with a significant rise in $i_{corrosion}$ and only marginal improvements in E and β_a, resulting in a 660 % increase in corrosion rate, although its corrosion tendency decreased slightly by 8 %. In contrast, Metglas showed a remarkably stable behavior. While some parameters such as β_a worsened slightly, the overall changes were minimal. The corrosion rate increased by only 13 %, and the corrosion tendency by 14 %, indicating that this alloy maintains good corrosion resistance even after thermal treatment. Most notably, FeNiCrSiB benefited from thermal treatment. The values of E, $i_{corrosion}$, and especially β_a improved significantly, with only a small decrease in R_p. This resulted in a 55 % reduction in corrosion rate and a 66 % decrease in corrosion tendency, confirming enhanced corrosion resistance post-treatment. These findings suggest that while thermal treatment may compromise corrosion resistance in some alloys, it can improve or preserve it in others—particularly FeNiCrSiB and Metglas. Therefore, for applications in aggressive environments, thermally treated Cr-rich alloys represent a promising solution due to their improved stability and resistance to corrosion.

4. Conclusions

This work has demonstrated that the self-bias effect, previously reported in Vitrovac® 7600 T70, can be successfully induced in other Fe-based magnetoelastic alloys, particularly in FeNiCrSiB, FeCoSiB, and Metglas alloys, through thermal annealing at 500 °C. All treated samples exhibited stable magnetoelastic resonances without the need for an external DC magnetic field, significantly simplifying the sensor configuration. Structural characterization via XRD and Mössbauer spectroscopy confirmed partial crystallization in all alloys, with the formation of Fe-based solid solutions responsible for the internal magnetic anisotropy that enables self-biasing. In addition, the treated sensors showed enhanced quality factors and improved frequency stability over time

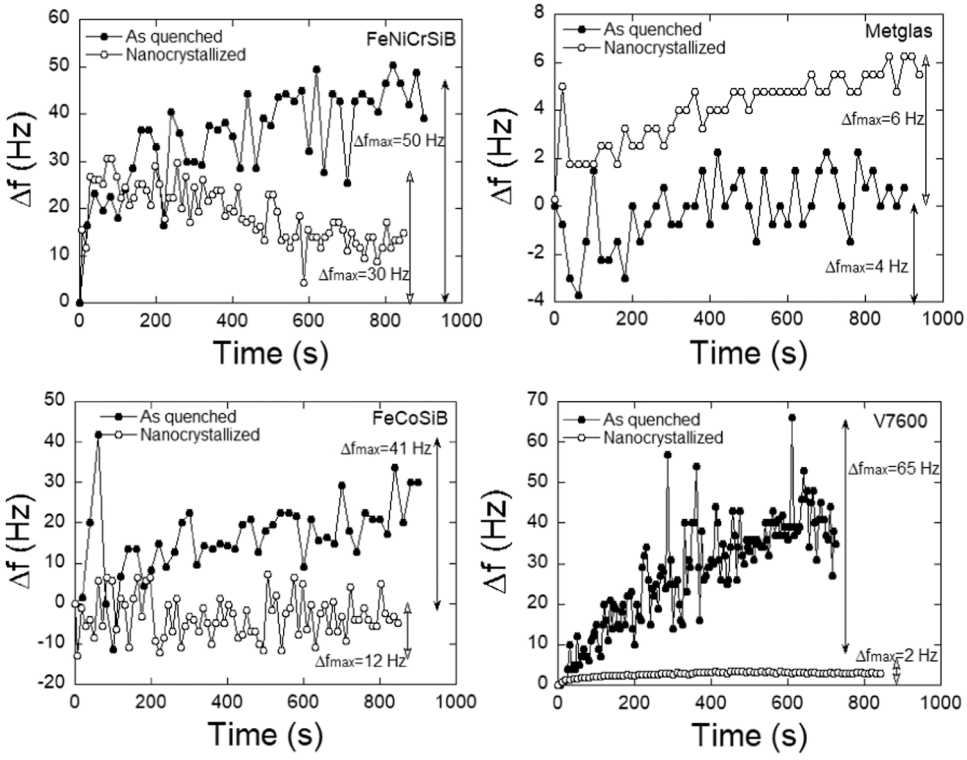

Fig. 8. Variation of the resonance frequency value over time of the as quenched and crystallized sensors.

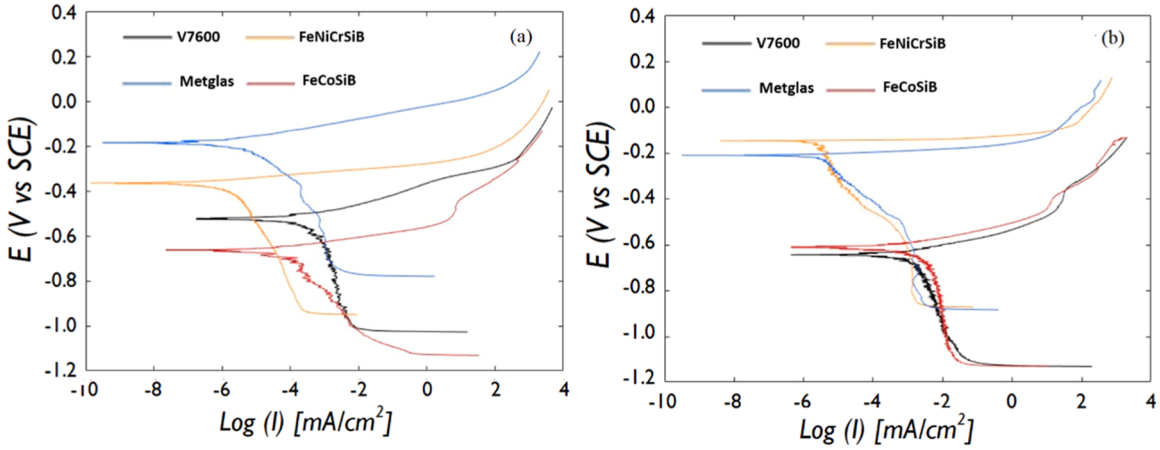

Fig. 9. Corrosion potential E as a function of the corrosion current density $I_{corrosion}$ for as quenched (a) and thermally treated (b) sensors.

compared to their as-quenched alloys. While Metglas and FeCoSiB produced higher ME signal amplitudes due to their greater amorphous fractions, the FeNiCrSiB and V7600 alloys exhibited better long-term signal stability. Importantly, the corrosion resistance evaluation revealed that thermal treatment deteriorated the corrosion performance of FeCoSiB and V7600, but had negligible effect on Metglas and led to a substantial improvement in FeNiCrSiB. These results confirm that Cr- and Ni-rich Fe-based alloys are promising platforms for the development of self-bias ME sensors, making them suitable candidates for their use in harsh or chemically aggressive environments.

CRediT authorship contribution statement

Ana Catarina Lopes: Writing – review & editing, Funding acquisition, Conceptualization. **Gutiérrez Jon:** Writing – review & editing, Funding acquisition. **García-Arribas Alfredo:** Writing – review & editing, Funding acquisition. **Aginagalde Andrea:** Writing – review & editing, Data curation. **Ayerdi Aitor:** Writing – review & editing, Data curation. **Quintana Iban:** Investigation. **Vilas José Luis:** Funding acquisition. **Saiz Garitaonandia José Javier:** Writing – review & editing, Writing – original draft, Investigation, Data curation, Conceptualization. **Lasheras Andoni:** Writing – review & editing, Writing – original draft, Investigation, Funding acquisition, Data curation, Conceptualization.

Declaration of Competing Interest

The authors declare that they have no known competing financial interests or personal relationships that could have appeared to influence the work reported in this paper.

Acknowledgements

A.C. Lopes acknowledges the Ramon y Cajal grant RYC2021–032277-I, funded by MICIU/AEI/10.13039/501100011033 and by European Union NextGenerationEU/PRTR. Authors are grateful to the Government of the Basque Country for financial support under Research Teams projects (IT1756–22 and IT1479–22) and Elkartek Program (MMASINT KK-2023/00041, FRONTIERS 2024 KK-2024/00099 and SMARTuS KK-2025/00120 projects). Authors want to thank as well the grant PID2023–150735OA-I00 funded by MICIU/AEI/10.13039/501100011033 and by ERDF/EU. Technical and human support provided by SGIKER (UPV/EHU, MICINN, GV/EJ, ERDF, and ESF) is also thankful.

Appendix A. Supporting information

Supplementary data associated with this article can be found in the online version at doi:10.1016/j.jallcom.2025.184229.

References

[1] P. G. Saiz, R. Fernández de Luis, A. Lasheras, M.I. Arriortua, A.C. Lopes, Magnetoelastic resonance sensors: principles, applications, and perspectives, ACS Sens. 7 (2022) 1248–1268, https://doi.org/10.1021/acssensors.2c00032.
[2] F. Ilgaz, E. Spetzler, P. Wiegand, F. Faupel, R. Rieger, J. McCord, B. Spetzler, Miniaturized double-wing ΔE-effect magnetic field sensors, Sci. Rep. 14 (2024) 11075, https://doi.org/10.1038/s41598-024-59015-5.
[3] W.S. Skinner, S. Zhang, R.E. Guldberg, K.G. Ong, Magnetoelastic sensor optimization for improving mass monitoring, Sensors 22 (2022) 827, https://doi.org/10.3390/s22030827.
[4] P. G. Saiz, D. Gandia, A. Lasheras, A. Sagasti, I. Quintana, M.L. Fdez-Gubieda, J. Gutiérrez, M.I. Arriortua, A.C. Lopes, Enhanced mass sensitivity in novel magnetoelastic resonators geometries for advanced detection systems, Sens. Actuators B Chem. 296 (2019) 126612, https://doi.org/10.1016/j.snb.2019.05.089.
[5] P.G. Saiz, J. Gutierrez, M.I. Arriortua, A.C. Lopes, Theoretical and experimental analysis of novel rhombus shaped magnetoelastic sensors with enhanced mass sensitivity, IEEE Sens. J. 20 (2020) 13332–13340, https://doi.org/10.1109/JSEN.2020.3006379.
[6] P.G. Saiz, J.M. Porro, A. Lasheras, R. Fernández de Luis, I. Quintana, M.I. Arriortua, A.C. Lopes, Influence of the magnetic domain structure in the mass sensitivity of magnetoelastic sensors with different geometries, J. Alloy. Compd. 863 (2021) 158555, https://doi.org/10.1016/j.jallcom.2020.158555.
[7] J. Winslow, V.E. Lamberti, M.P. Palmer, J.C. Tokash, M. DeVinney, T. Dallas, Miniaturized magnetoelastic sensor system, IEEE Sens. J. 24 (2024) 15975–15985, https://doi.org/10.1109/JSEN.2024.3379880.
[8] I.Y. Choi, J. Choe, B.A. Chin, M.-K. Park, User-friendly, signal-enhanced planar spiral coil-based magnetoelastic biosensor combined with humidity-resistant phages for simultaneous detection of salmonella typhimurium and escherichia coli O157:H7 on fresh produce, Sens. Actuators B Chem. 393 (2023) 134179, https://doi.org/10.1016/j.snb.2023.134179.
[9] A. Lasheras, J.S. Garitaonandia, I. Quintana, J.L. Vilas, A.C. Lopes, Development of nanocrystallized magnetoelastic sensors with self-biased effect and improved mass sensitivity, Sens. Actuators Rep. 8 (2024) 100251, https://doi.org/10.1016/j.snr.2024.100251.
[10] S. Sang, S. Gao, X. Guo, P. Cheng, W. Zhang, The detection of Pb2+ in solution using bare magnetoelastic resonator, Appl. Phys. Lett. 108 (2016), https://doi.org/10.1063/1.4941024.
[11] P. G. Saiz, R. Fernández de Luis, L. Bartolome, J. Gutiérrez, M.I. Arriortua, A. C. Lopes, Rhombic-magnetoelastic/metal–organic framework functionalized resonators for highly sensitive toluene detection, J. Mater. Chem. C. 8 (2020) 13743–13753, https://doi.org/10.1039/D0TC02612C.
[12] X. Guo, J. Wang, Y. Zhao, R. Liu, Q. Zhang, Z. Yuan, S. Sang, A wireless magnetoelastic DNA-biosensor amplified by AuNPs for the detection of a common mutated DNA causing β-thalassaemia, Biochem. Eng. J. 156 (2020) 107498, https://doi.org/10.1016/j.bej.2020.107498.
[13] S. Sang, X. Guo, J. Wang, H. Li, X. Ma, Real-time and label-free detection of VKORC1 genes based on a magnetoelastic biosensor for warfarin therapy, J. Mater. Chem. B. 8 (2020) 6271–6276, https://doi.org/10.1039/D0TB00354A.
[14] S. Shekhar, S.S. Karipott, R.E. Guldberg, K.G. Ong, Magnetoelastic sensors for real-time tracking of cell growth, Biotechnol. Bioeng. 118 (2021) 2380–2385, https://doi.org/10.1002/bit.27680.

[15] X. Gao, W. Yang, P. Pang, S. Liao, Q. Cai, K. Zeng, C.A. Grimes, A wireless magnetoelastic biosensor for rapid detection of glucose concentrations in urine samples, Sens. Actuators B Chem. 128 (2007) 161–167, https://doi.org/10.1016/j.snb.2007.05.045.
[16] P.G. Stoyanov, C.A. Grimes, A remote query magnetostrictive viscosity sensor, Sens. Actuators A Phys. 80 (2000) 8–14, https://doi.org/10.1016/S0924-4247(99)00288-5.
[17] I. Bravo, A. Arnaiz, A. Garcia-Arribas, Damping of magnetoelastic resonance for oil viscosity sensing, IEEE Trans. Magn. 55 (2019) 1–5, https://doi.org/10.1109/TMAG.2018.2873248.
[18] B. Sisniega, A. Sagasti Sedano, J. Gutiérrez, A. García-Arribas, Real time monitoring of calcium oxalate precipitation reaction by using corrosion resistant magnetoelastic resonance sensors, Sensors 20 (2020) 2802, https://doi.org/10.3390/s20102802.
[19] A. Sagasti, A.C. Lopes, A. Lasheras, V. Palomares, J. Carrizo, J. Gutierrez, J. M. Barandiaran, Corrosion resistant metallic glasses for biosensing applications, AIP Adv. 8 (2018), https://doi.org/10.1063/1.4994108.
[20] B. Sisniega, R. Fernández de Luis, J. Gutiérrez, A. García-Arribas, Magnetoelastic resonators functionalized with metal–organic framework water harvesters as wireless humidity sensors, APL Mater. 12 (2024), https://doi.org/10.1063/5.0206165.
[21] B. Sisniega, J. Gutiérrez, J.M. Barandiaran, J.M. Porro, A. García-Arribas, Influence of magnetic relaxation on magnetoelastic resonance-based detection, J. Phys. D. Appl. Phys. 56 (2023) 105001, https://doi.org/10.1088/1361-6463/acba29.
[22] A. Lasheras, P.G. Saiz, J.M. Porro, I. Quintana, C. Polak, A.C. Lopes, Enhanced performance of magnetoelectric laminated composites by geometry engineering for high frequency applications, J. Alloy. Compd. 884 (2021) 161065, https://doi.org/10.1016/j.jallcom.2021.161065.
[23] R.A. Brand, Normos Mössbauer fitting program, Univ. Duisbg, 2002.
[24] I. Bibicu, J. Garitaonandia, F. Plazaola, E. Apiñaniz, X-ray diffraction, transmission Mössbauer spectrometry and conversion electron Mössbauer spectroscopy studies of the Fe87Zr6B6Cu1 nanocrystallization process, J. Non Cryst. Solids 287 (2001) 277–281, https://doi.org/10.1016/S0022-3093(01)00589-0.
[25] H. Nam Ok, A.H. Morrish, Surface crystallization and magnetic anisotropy in amorphous Fe40Ni38Mo4B18 ribbons, J. Appl. Phys. 52 (1981) 1835–1837, https://doi.org/10.1063/1.329544.
[26] K.K. Kadyrzhanov, V.S. Rusakov, M.S. Fadeev, T.Y. Kiseleva, A.L. Kozlovskiy, I. E. Kenzhina, M.V. Zdorovets, Study of magnetic properties of Fe100-xNix nanostructures using the Mössbauer spectroscopy method, Nanomaterials 9 (2019) 757, https://doi.org/10.3390/nano9050757.
[27] R. Parsons, J.S. Garitaonandia, T. Yanai, K. Onodera, H. Kishimoto, A. Kato, K. Suzuki, Effect of si on the field-induced anisotropy in Fe-rich nanocrystalline soft magnetic alloys, J. Alloy. Compd. 695 (2017) 3156–3162, https://doi.org/10.1016/j.jallcom.2016.11.330.
[28] K. Suzuki, N. Ito, J.S. Garitaonandia, J.D. Cashion, G. Herzer, Local random magnetocrystalline and macroscopic induced anisotropies in magnetic nanostructures, J. Non Cryst. Solids 354 (2008) 5089–5092, https://doi.org/10.1016/j.jnoncrysol.2008.06.118.
[29] X. Wu, S.-J. Bu, X.-H. Han, C. Zhang, J.-B. Sun, Y. Zhang, Y.-F. Pan, Effects of si and/or ti addition on the microstructure and magnetic properties of Fe–Cr–Co ribbons, IEEE Trans. Magn. 53 (2017) 1–8, https://doi.org/10.1109/TMAG.2016.2645897.
[30] L. Wang, Z. Zheng, Y. Chen, X. Chen, Z. Qiu, D. Zeng, S. Yuan, The influence of co on the magnetic properties of Fe–Si–B–Nb–Cu system, Phys. B Condens. Matter. 660 (2023) 414906, https://doi.org/10.1016/j.physb.2023.414906.
[31] P. Kwapuliński, G. Haneczok, Magnetic relaxation in iron based melt spun ribbons, Acta Phys. Pol. A. 136 (2019) 701–704, https://doi.org/10.12693/APhysPolA.136.701.